Journal of The
Electrochemical Society

Ni- and Sb-Doped SnO_2 Electrocatalysts with High Current Efficiency for Ozone Production via Electrodeposited Nanostructures

To cite this article: Cassandra M. Lees *et al* 2018 *J. Electrochem. Soc.* **165** E833

Journal of The Electrochemical Society, **165** (16) E833-E840 (2018)
0013-4651/2018/165(16)/E833/8/$37.00 © The Electrochemical Society

Ni- and Sb-Doped SnO_2 Electrocatalysts with High Current Efficiency for Ozone Production via Electrodeposited Nanostructures

Cassandra M. Lees, James L. Lansing, Samantha L. Morelly, Sophia E. Lee,* and Maureen H. Tang[z]

Department of Chemical and Biological Engineering, Drexel University, Philadelphia, Pennsylvania 19104, USA

Ozone is a powerful disinfectant in water treatment, and electrochemical ozone production (EOP) is desirable because it can be safer than current production methods. The greatest challenge for electrochemical ozone production is the lack of catalysts with high selectivity for ozone evolution. Nickel- and antimony- doped tin oxide electrodes synthesized from sol-gels and nanoparticles have been reported to reach ozone current efficiencies up to 50% for electrochemical ozone production. In this study, we present a novel electrodeposition synthesis method that results in current efficiencies up to 63%. The optimal temperature of the post-deposition oxidation treatment is determined by the tradeoff between catalyst stability and crystallinity. Analysis via microscopy and X-ray diffraction suggests that electrodeposited films provide sufficient Ni concentration, surface area, and morphology to support a solution-mediated ozone production reaction.
 [DOI: 10.1149/2.0051816jes]

Manuscript submitted July 3, 2018; revised manuscript received October 8, 2018. Published November 27, 2018.

Ozone is a powerful oxidant that kills microorganisms, decomposes organic molecules, and removes unwanted components including coloration, cyanide, phenols, iron, and manganese.[1] It can be used to disinfect portable water, food, surgical equipment, and sewage, and in manufacturing, pure water is needed in semiconductor production, pharmaceutical production, and biotechnology.[2] Additionally, ozone is safer than many other disinfectants because it decays to oxygen relatively quickly and leaves no harmful residuals. The current method of ozone production is cold corona discharge, which either produces harmful nitrogen oxides or requires additional equipment and expense for separating pure oxygen from air. Furthermore, the maximum ozone concentration achievable via cold corona discharge is 10 wt%, which is relatively low and can result in low operational efficiency.[3] To avoid harmful NO_x, expensive pure oxygen, low ozone concentrations, and slow dissolution times, growing attention has focused on electrochemical ozone production (EOP) from water electrolysis.[4–7]

The greatest challenge to EOP is selectivity. Water is much more readily oxidized to oxygen than ozone because oxygen evolution is thermodynamically favorable at a lower anodic potential.

$$2H_2O \rightarrow O_2 + 4H^+ + 4e^- \quad E^\circ = 1.23V \text{ vs RHE} \qquad [1]$$

$$3H_2O \rightarrow O_3 + 6H^+ + 6e^- \quad E^\circ = 1.56V \text{ vs RHE} \qquad [2]$$

Various electrocatalytic parameters have been investigated to try to encourage ozone evolution, retard oxygen evolution, and understand the mechanisms of selectivity. Parameters including anodic materials, electrode morphology, cell configurations, current density, electrolyte, anodic potential, and temperature have been investigated.[3,5–8] Of the materials investigated, nickel- and antimony-doped tin oxide (NATO) has gained attention as an EOP catalyst due to its low cost and low toxicity. It was first identified for EOP in 2005 by Wang et al., who studied the effect of Sn:Sb:Ni ratio, cell potential, and electrolyte on current efficiency in a closed cell. Wang showed a maximum current efficiency of 36%,[8] while Christensen et al. further optimized Wang's Sn:Sb:Ni ratio and cell potential under flow conditions, reaching current efficiencies up to 50%.[9] These studies and others have also addressed NATO's poor stability. In 2013, Wang et al. developed a fluoride-doped tin oxide interlayer that increased the lifetime of NATO by a factor of six,[10] and Parsa et al. attempted to increase the catalyst's stability by synthesizing a composite containing sol-gel NATO and carbon nanotubes. This yielded stable yet low current efficiencies between 20–30%.[11] More recently, Christensen et al. synthesized nanopowder NATO to investigate the role of dopants. They proposed an EOP mechanism with multiple adsorbed intermediates, yielding stable current efficiencies between 10 and 20%.[12]

In nearly all reports, NATO has been synthesized by various sol-gel methods.[4,8] However, electrodeposition is an alternative synthetic route that can yield very rough, nanostructured surfaces with a high density of active sites. In this study, we explore the viability of this method for synthesizing EOP catalysts. We show that electrodeposition followed by thermal oxidation can yield NATO catalysts with high current efficiency for ozone production. The effects of thermal oxidation temperature on activity, current efficiency, crystal structure, and morphology are observed and discussed. Furthermore, we show that the ozone current efficiency, as well as activity, is sensitive to catalyst loading, suggesting that the EOP reaction on NATO goes through a solution – mediated intermediate.

Experimental

Material synthesis.—5 × 10mm Ti foil (0.25mm thick, 99.7%, Sigma Aldrich) was boiled in 10 wt% oxalic acid (Alfa Aesar) for 10 minutes then rinsed with Millipore water and dried at room temperature. The electrodeposition protocol was modified from Hu et al.'s preparation of SnO_2 nanoparticle films.[13] A solution of 0.1 M KCl (>99%, Sigma Aldrich), 0.1 M HCl (37%, Sigma-Aldrich), 0.05 M $SnCl_2$ (Anhydrous, 98%, Alfa Aesar), 0.05 M $SbCl_3$ (>99%, Sigma Aldrich), and 0.05 M $NiCl_2 \cdot 6H_2O$ (Sigma Aldrich) was held at 90 degrees in an unstirred, unseparated cell. To maintain uniform current distributions and avoid edge effects, the counter and working electrodes were aligned in parallel and the working electrode was masked to be slightly smaller than the counter electrode. These efforts were necessary to maintain reproducibility between sister samples. A pulse of −20 mA/cm^2 for 30 seconds was followed by relaxation at 0 mA/cm^2 for 10 seconds for a fixed number of cycles. The electrodeposition bath pH was measured to be 1.36, the cell potential during pulses was around −0.22 V vs RHE, and the counter electrode was also Ti foil (0.25 mm thick, 99.7%, Sigma Aldrich). Potentials were monitored vs an Ag/AgCl reference electrode (BASi). After electrodeposition, the anodes were rinsed in Millipore water and either stored at room temperature or thermally oxidized in air at 300, 450, or 600°C for two hours in a muffle furnace (Thermolyne).

As a control to compare current efficiencies of different synthesis methods, NATO samples were made via sol-gel synthesis similar to Wang et al and Christensen et al.[8,9] 1.0 M $SnCl_4 \cdot 5\ H_2O$ (98%, Sigma Aldrich), 0.064 M $SbCl_3$ (>99%, Sigma Aldrich), and 0.008 M $NiCl_2 \cdot 6H_2O$ (Sigma Aldrich) in ethanol (200 proof, anhydrous, Decon Labs) was chosen based on the optimal performance of electrodes in Christensen's 2009 study.[9] Ti foils were prepared as described above. To control catalyst loading, each sample remained in

*Electrochemical Society Student Member.
[z]E-mail: mhtang@drexel.edu

a muffle furnace at 500°C and 15 µl /cm^2 of the ethanol solution was drop-casted on the exposed surface. Samples were heated for 10 minutes between coats and seven coats were applied, for a calculated total film thickness of about 20 µm. Samples were then thermally oxidized at 500°C in air for two hours.

Characterization.—Electrodeposited samples were characterized with X-ray diffraction (XRD) using Cu K-α radiation at 40 kV and 30 mA between 20 and 80 2θ (Rigaku SmartLab), scanning electron microscopy (SEM, Zeiss Supra 50VP), and energy dispersive X-ray spectroscopy (EDS). SEM images were taken at a working distance of 12 mm and a working voltage of 3–5 keV. EDS was performed at a working distance of 12 mm, a working voltage of 10 keV. Composition was averaged over 8 scans of a 10 × 15 µm area. X-ray photoemission spectroscopy (XPS) measurements were performed with a Versa Probe 5000 spectrometer (Physical Electronics Inc., USA) with monochromatic Al Kα radiation and a beam setting of 100 µm with 25 W and 15kV. Ion sputtering was carried out using a 0.5KeV Ar+ ion gun for 12 minutes. Elemental composition was averaged from survey spectra collected at three locations on each sample. For Sb, the Sb $3d_{5/2}$ orbital at 530eV overlaps with O 1s at 531eV, so Sb $3d_{3/2}$ at 539eV was used for determining composition and peak fitting. Ni was fit based on the Ni 2p peak at 855eV and Sn was fit based on the Sn3d peak at 488.5eV. Adventitious carbon C1s at 284.5eV was used for charge correction. For Sn, peak splitting of 8.4eV was used and the binding energy of the $Sn3d_{5/2}$ orbital was assumed to be 485.2, 486 and 486.6 eV for Sn, Sn^{2+} and Sn^{4+} respectively. For Sb, a peak splitting of 9.4eV was used and the binding energy of the $Sb3d_{3/2}$ orbital was assumed to be 537.7, 539.3 and 540.3 eV for Sb, Sb^{3+} and Sb^{5+} respectively.

Electrochemical testing and current efficiency.—Methods were adapted from Wang et al. The working, Pt wire counter (Sigma Aldrich), and Ag/AgCl reference (BASi) electrodes were placed in a sealed 4.5 mL quartz cuvette containing 0.5 M H_2SO_4 and then connected to a Biologic potentiostat.[8] The electrolyte pH was measured to be 0.84, and fresh solution was used for each test. Current and ozone concentration were measured at constant polarization of 2.75 V vs RHE with iR compensation for 60 seconds. To measure ozone concentration in-situ, a Perkin-Elmer Lambda 35 UV/VIS spectrometer recorded absorbance at 258 nm during potentiostatic testing. The spectrometer absorbance background was corrected immediately before the start of each test. Concentration was determined from absorbance via Beer's law with the molar extinction coefficient of 3000 $M^{-1}cm^{-1}$ recommended by the International Ozone Association.[14] Ozone current efficiency (φ) was calculated from an integrated form of Faraday's law:

$$\varphi = \frac{6 \cdot F \cdot c_{O3} \cdot V_{cell}}{Q} \quad [3]$$

The ozone concentration estimated from the in-situ measurement was verified via the well-known indigo method for ozone quantification.[15] 0.00125 M potassium indigo trisulfonate (Sigma Aldrich) was prepared in solution of Millipore water and 85 wt% phosphoric acid (Sigma Aldrich) as a stock solution. 200 µl of stock solution was diluted 50x with Millipore water and mixed with sodium phosphate monobasic buffer (>99%, Sigma Aldrich) and 85 wt% phosphoric acid (Sigma Aldrich) to make the final.24 µM indigo reagent. Just prior to ozone synthesis, a disposable cuvette was prepared with 2.0 ml of reagent. At the appropriate time, a 0.133 ml aliquot was quickly extracted from the quartz cuvette and mixed with the reagent in the disposable cuvette. Because indigo trisulfonate reacts stoichiometrically with ozone, the moles of indigo that were consumed after the addition of the aliquot were attributed to an equal number of moles of ozone. Current efficiency was then calculated from ozone concentration in the aliquot via Equation 3, again assuming that ozone decomposition and escape from the cuvette were negligible.

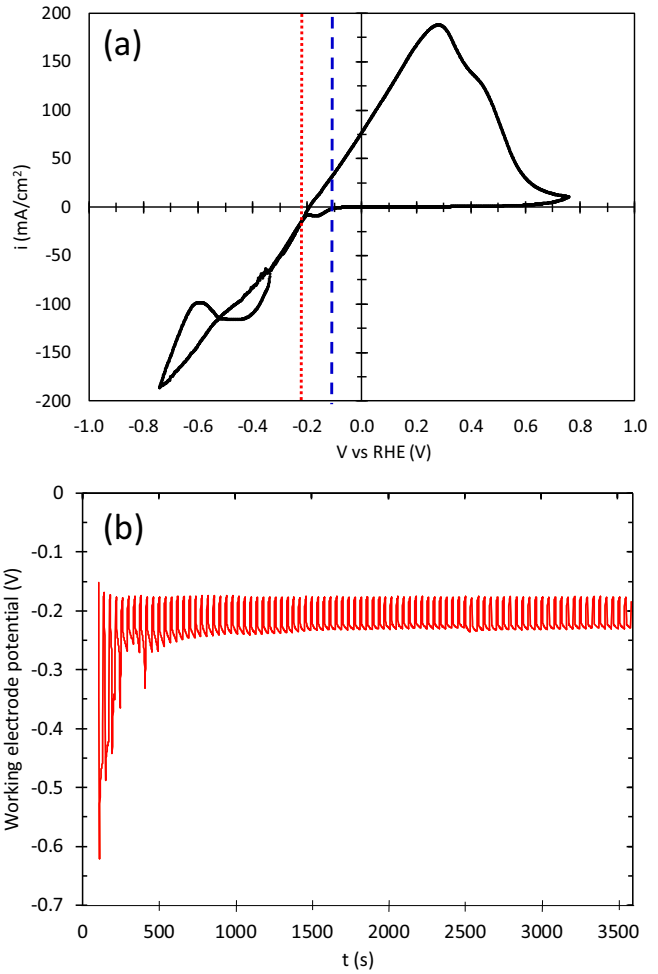

Figure 1. (a) 20 mV/s CV of electrodeposition bath vs. RHE. The vertical lines show the reduction potentials for Sn^{2+}/Sn (blue, −0.103 V) and Ni^{2+}/Ni (red, −0.217 V). (b) Working electrode potential during 90 cycles of a 30 second −20 mA/cm2 pulse and a 10 second relaxation.

Results and Discussion

Electrodeposition.—Electrodeposition of mixed metals and alloys has been documented for dozens of alloying groups in aqueous media.[16,17] At low potential, Sn^{2+} and Ni^{2+} ions are directly reduced to Sn and Ni. At low pH in aqueous solutions, Sb is typically present as SbO^+.[18] At pH of 1.36, ion concentration of 0.05M, and temperature of 90°C, the thermodynamic reduction potentials are:

$$Sn^{2+} + 2e^- \rightarrow Sn \quad \text{U} = -0.103 \text{ V vs RHE} \quad [4]$$

$$Ni^{2+} + 2e^- \rightarrow Ni \quad \text{U} = -0.217 \text{ V vs RHE} \quad [5]$$

$$SbO^+ + 3e^- + 2H^+ \rightarrow Sb + H_2O \quad \text{U} = 0.188 \text{ V vs RHE} \quad [6]$$

A 20 mV/s CV of a Ti substrate in the electrodeposition solution (Figure 1a) shows the potentials at which reactions occur in the electrodeposition bath. Definitive assignment of the peaks is difficult due to large activation and concentration overpotentials in this system. However, the small peak at approximately −0.1 V occurs at the expected value for Sn electrodeposition, while the larger reduction peak at −0.36 may indicate Ni electrodeposition. Although Sb is the most noble of the three metals, $SbCl_3$ hydrolyzes rapidly in aqueous solution such that deposition is less facile than either Ni or Sn. The large

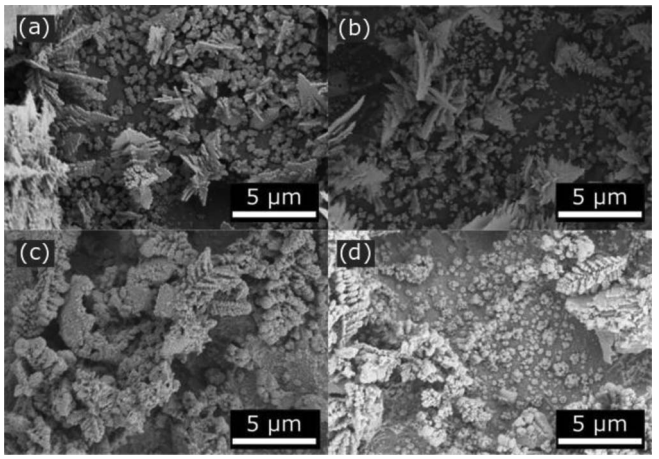

Figure 2. SEM images of electrodeposited NATO after (a) no thermal oxidation, (b) 300°C, (c) 400°C, and (d) 600°C oxidation. Electrodes were formed with 90 electrodeposition cycles.

wave at −0.7 V is attributed to hydrogen evolution; at such low potentials, bubbles appeared visibly at the cathode. On the anodic sweep, the newly-deposited metal was electrochemically oxidized, as shown by the large positive peak at 0.30 V. We emphasize that the focus of this work is not an in-depth study of the electrodeposition of the complicated Ni-Sb-Sn system,[19–21] but rather the impact of the dendritic electrodeposited structure on the current efficiency for ozone production and its implications for the reaction mechanism. As such, detailed mapping of the voltammetry peaks to specific deposition reactions is beyond the scope of the present work. Figure 1b shows potential during the pulse deposition. After the first few deposition cycles, the potential of the working electrode is between −0.17 and −0.25 V vs RHE, at which deposition of all three metals is thermodynamically favored.

After pulse electrodeposition, anodes were thermally oxidized at 300°C, 450°C, or 600°C. As-deposited samples are denoted as 90°C, the temperature of the electrodeposition bath. Representative SEM images of after thermal oxidation are shown in Figure 2. Figure 2a shows the formation of thin, metallic dendrites. Oxidation at 300°C has little effect (Figure 2b), but oxidation at 450° and 600°C causes visible swelling due to oxygen incorporation into the structure (Figures 2c, 2d). Although the rough and nonuniform morphologies in Figure 2 are undesirable in traditional applications of electrodeposition, electrocatalysts perform best with high surface areas that maximize the number of active sites. Dendritic structures such as those in Figure 2 can be ideal for this purpose.

X-ray diffraction was performed to identify bulk phases at different thermal oxidation temperatures utilizing the Crystallography Open Database, as shown in Figure 3.[22–26] Ni, Ti, different oxidation states of Sn, and several Ni-Sn intermetallics are present at every temperature. Figure 3a shows an XRD pattern of an as-plated NATO sample. There are intense peaks attributed to the Ti substrate, metallic Sn and Ni, as well as SnO and a Ni_3Sn intermetallic. Figure 3b shows the XRD pattern of an electrodeposited sample after 300°C thermal

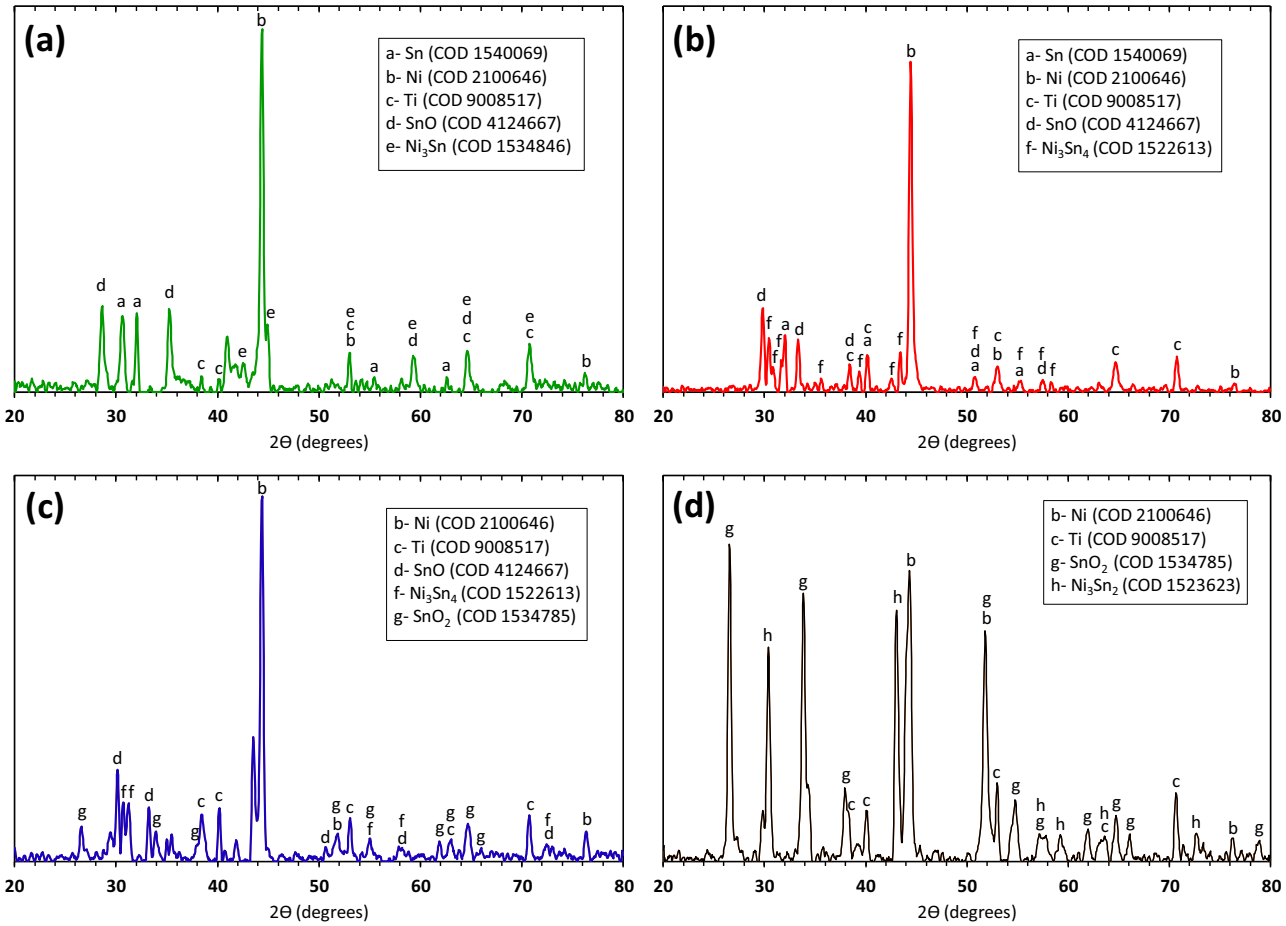

Figure 3. XRD of 90-cycle electrodeposited NATO after: (a) electrodeposition at 90°C. Phases present include Sn, Ni, Ti, SnO, and Ni_3Sn. (b) 300°C thermal oxidation. Phases present include Sn, Ni, Ti, SnO, and Ni_3Sn_4. (c) 450°C thermal oxidation. Phases present include Ni, Ti, SnO, Ni_3Sn_4, and SnO_2. (d) 600°C thermal oxidation. Phases present include Ni, Ti, SnO_2, and Ni_3Sn_2.

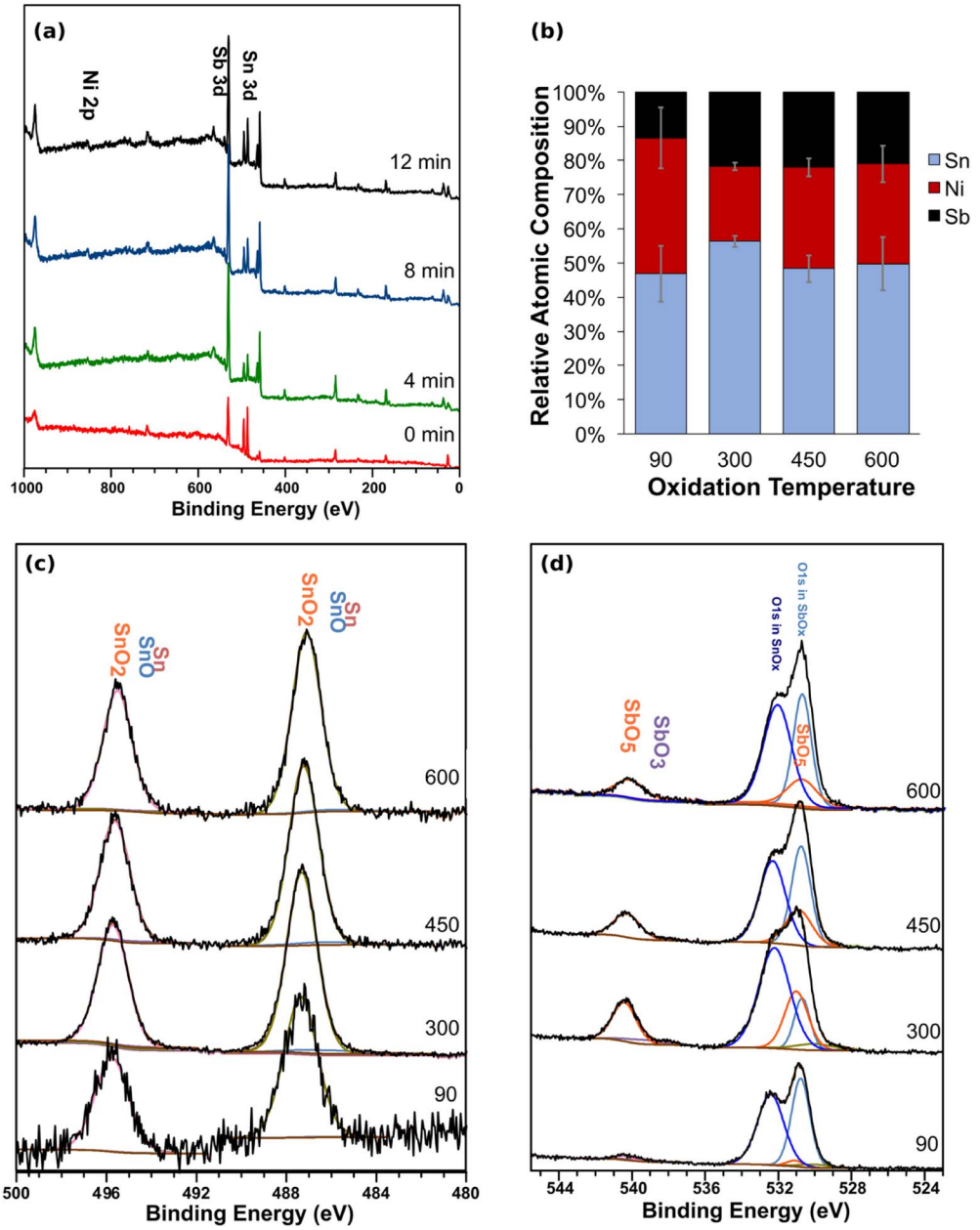

Figure 4. XPS of electrodeposited NATO as-deposited and after 300°C, 450°C, and 600°C oxidation. (a) Characteristic XPS spectra after 0, 4, 8, and 12 minutes of sputtering with 0.5 keV Ar^+ ion gun. (b) Average composition of Ni, Sb, and Sn calculated from XPS spectra. (c, d) Detailed elemental spectra for Sn and Sb respectively.

oxidation in air for 2 hours. The Sn, Ni, Ti, and SnO peaks are still apparent after thermal oxidation, however the Ni_3Sn peak disappears and is replaced by Ni_3Sn_4. Figure 3c shows a sample after 450°C thermal oxidation in air for 2 hours. The appearance of SnO_2 in Figure 3c corresponds to the disappearance of the Sn peak and the visual observation of mossy oxides in Figure 2c. The Ni, Ti, SnO, and Ni_3Sn_4 peaks remain. Figure 3d shows the XRD pattern after 600°C thermal oxidation. The intermetallic Ni_3Sn_4 disappears and is replaced by Ni_3Sn_2, SnO disappears, and the Ni, Ti, and SnO_2 still remain. The Ni peak appears less intense compared to the SnO_2 and Ni_3Sn_2 peaks, likely because the higher oxidation temperatures lead to increased Ni mixing. Although the formation of amorphous NiO_x is also possible, crystalline Ni oxides such as NiO and Ni_2O_3 were not observed at any temperature.

The compositions of the electrodes were measured with XPS. Ni dissolves in strong acid, and initial survey spectra of all samples showed an absence of Ni. However, mild ion sputtering revealed subsurface Ni across all samples (Figure 4a). Although the Ni signal was apparent after only 4 minutes of sputtering, a sputtering time of 12 minutes was chosen for analysis to ensure consistent comparisons across samples. Relative atomic compositions calculated from XPS showed no trend in composition with thermal oxidation temperature (Figure 4b). Detailed elemental spectra showed similar oxidation states at all temperatures for both Sn and Sb, with Sb^{5+} and Sn^{4+} as the dominant oxidation states (Figures 4c, 4d). The presence of Sb^{5+} and Sn^{4+} on the samples with bulk Sn metal and no bulk SnO_2 shows the presence of native oxides before thermal oxidation at elevated temperature.

Electrochemical performance.—Electrochemical performance and ozone current efficiency were measured in-situ via direct absorbance at 258 nm as well as ex-situ with the indigo method. Cyclic

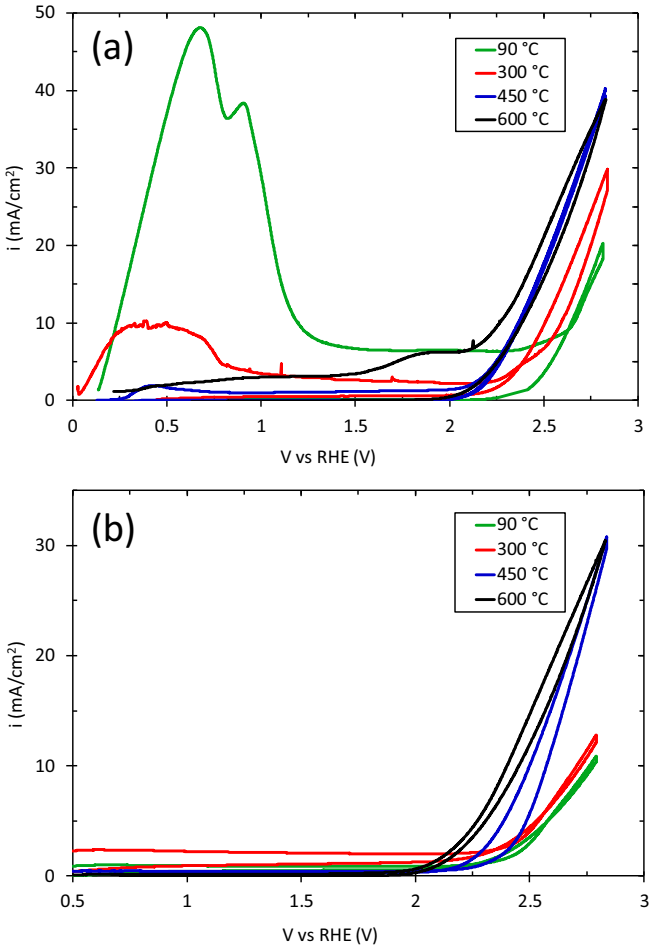

Figure 5. CV at 50 mV/s in 0.5M H_2SO_4 for NATO samples prepared at different thermal oxidation temperatures. The peaks between 0.4 and 0.7 V present in the first cycle (a) are not present in the second cycle (b) or other subsequent cycles, suggesting irreversible oxidation of residual metals.

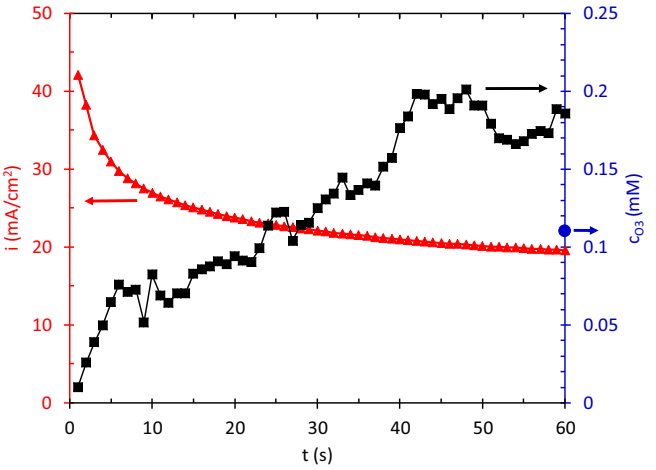

Figure 6. Time dependence of ozone concentration and current density of a NATO sample thermally oxidized at 600°C after 60 cycles of electrodeposition. Ozone concentration calculated via the in-situ method is shown in black, and final ozone concentration calculated via the indigo method is shown at 60 seconds in blue. The sol-gel control measured a concentration of 0.2 mM O_3 in-situ, and 0.13 mM O_3 via the indigo method.

voltammograms at 50 mV/s were recorded initially to estimate electrocatalytic activity as shown in Figure 5. Potential was swept from open circuit potential to 2.75 V vs RHE at 50 mV/s. Figure 5a shows the first cycle for different oxidation temperatures. All the samples showed water oxidation beginning around 2.0 V vs RHE. A current peak between 0.4 and 0.7 V was also observed on the first cycle only. This peak current decreased with higher oxidation temperatures and is attributed to the electrochemical oxidation of residual Sn and Ni. After the first cycle the peak disappeared (Figure 5b), consistent with irreversible oxidation of Sn metal to SnO_2 and dissolution of Ni to soluble Ni^{2+}. In acid, Ni is thermodynamically stable at high potentials as a dissolved cation, but Ni stability in the SnO_2 lattice after polarization has been reported.[27]

After initial voltammetry, the electrode was polarized potentiostatically at 2.75 V vs RHE while recording absorbance at 258 nm. Figure 6 shows both the current and the ozone concentration, calculated directly from the absorbance at 258 nm and Beer's Law, during electrolysis. The calculated concentration reaches a plateau or steady-state, presumably due to consumption of ozone at the counter electrode or loss from imperfect sealing of the cuvette. This steady state is not due to the solubility limit for ozone. The solubility of ozone in water is 2.3 mM (109 mg/L), and the highest concentration observed in this study across all samples was 1.2 mM. The plateau in concentration was observed in almost all samples, including those with much lower concentrations. For comparison, the solubility of oxygen is 8 mg/L or 0.25 mM. To calculate the current efficiency from the in-situ method, Equation 3 was applied to the integrated charge at the time at which concentration appeared to reach steady-state. In Figure 6, this corresponds to a time of 45 seconds.

The current efficiency measured for the 450°C sample by the in-situ method was 31%, which corresponds with other NATO samples in literature.[8,9,11,28] The average current efficiency determined by this method for the sol-gel control was 32%. The characteristic odor of ozone was also observed upon opening the cuvette. However, the direct absorbance at 258 can be subject to interference, and obtaining a calibration curve with solutions of known ozone concentration is experimentally challenging. To verify the ozone concentration calculated at 258 nm, the indigo method was performed. This method underestimates ozone concentration because it does not account for decomposition at the counter electrode or escape from the cuvette. However, it much less sensitive to local concentration gradients that may form during electrolysis and to optical interference. Figure 7 shows (a) the UV-vis spectra for different concentrations of indigo trisulfonate and (b) the resulting calibration curve. The empirically determined molar extinction coefficient of 20100 $M^{-1}cm^{-1}$ is in good agreement with the accepted value of 20000 $M^{-1}cm^{-1}$.[15] As shown by the blue marker in Figure 6, the resulting ozone concentration calculated from indigo consumption after introduction of reacted electrolyte was lower than that measured in-situ, but in reasonable agreement. For the sol-gel control, the average current efficiency via the indigo method was 22%.

Both morphology and crystal structure are affected by thermal oxidation temperature and are expected to have significant impact on electrochemical performance. The effect of increasing oxidation temperature on ozone current efficiency (Figure 8) and total current density (Figure 9) as measured by both methods is examined. Data points represent an average of three samples and the error bars reflect one standard deviation in each direction. Both current density and ozone current efficiency are similar between 90°C and 300°C, reach a maximum at 450°C, and then decrease when temperature increases to 600°C. The two methods for ozone concentration measurement agree qualitatively, although the indigo method yields higher ozone concentrations for less active samples and lower concentrations for more active samples. Scatter is highest for the in-situ method on samples with higher current efficiency. We hypothesize that the UV-vis beam, which travels directly above the working electrode, may be sampling a region of higher or lower concentration than

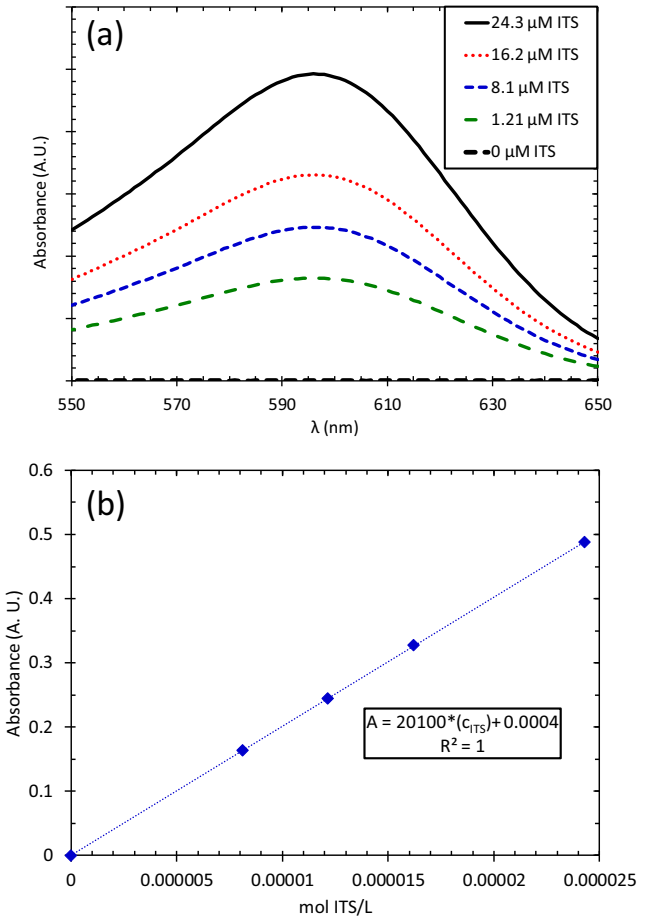

Figure 7. (a) UV-VIS absorbance spectra for different concentrations of indigo trisulfonate. (b) Calibration curve to determine molar extinction coefficient.

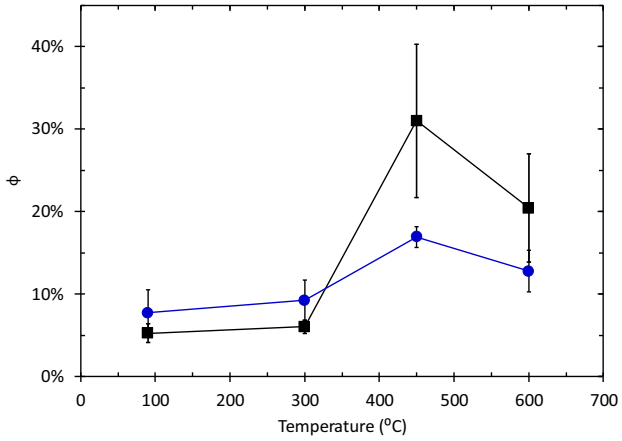

Figure 8. Average current efficiency vs. thermal oxidation temperature calculated using the in-situ method (black squares) and the indigo method (blue circles) for the same samples. Measurements reflect the average of three independently synthesized samples with 60 electrodeposition cycles. Sol-gel controls yielded an average of 32% current efficiency via the in-situ method and 22% via the indigo method.

the average. If so, it is therefore sensitive to the convection pattern in the cuvette, including the formation of oxygen and ozone bubbles.

The increased current efficiency at 450°C corresponds to the appearance of crystalline SnO_2 in XRD and mossy structures in SEM, implying that the crystalline SnO_2 formed via thermal oxidation is more active for ozone production than the amorphous SnO_2 that is formed from electrochemical oxidation. The selectivity of the amorphous SnO_2 for oxygen evolution and catalyst dissolution is consistent with observations of Danilovic et al, who observed higher oxygen evolution activity and lower electrochemical stability on electrochemically oxidized metals compared to thermally oxidized metals. They proposed that this difference is due to the higher defect concentrations in the electrochemically formed oxide, compared to the crystalline thermal oxide.[29] However, the 600°C samples with even higher SnO_2 crystallinity exhibit lower ozone current efficiency than the 450°C samples. The 450°C maximum corresponds to Christensen et al.'s observations on sol-gel-synthesized NATO, which were attributed to a more optimal defect structure.[27] Similarly, Fabbri et al studied Sb-SnO_2 supports for fuel cells and found that higher temperature resulted in surface segregation of Sb and lower electronic conductivity,[30] which would explain the decreased current density at 600°C. However, it is not obvious why a more resistive catalyst would affect selectivity more than activity. As a third consideration, the oxidation temperature may affect ozone activity via the Ni concentration. Wang et al. and Christensen et al. both studied the effect of Sn:Ni ratio on ozone current efficiency.[27,28] Ni concentration was shown to have a strong effect on current efficiency, with Wang's Sn: Ni optimal ratio being 500:1 and Christensen's Sn: Ni ratio being 500:3. From the XPS of Figure 4b, the Sn:Ni ratio is 2:1, but XRD shows that the Ni is present in a variety of pure and alloyed phases. At 600°C, it is possible that higher atomic mobility incorporates so much Ni into the SnO_2 structure that the optimum Ni dopant concentration is no longer present in the SnO_2 lattice.

To characterize the stability of the materials, SEM /EDS was performed after ozone production for 60 seconds at 2.75 V vs RHE. SEM images after testing are shown in Figure 10. The impact of metal oxidation on current density and current efficiency at low temperatures is supported by the SEM images of samples measured after ozone electrolysis. Figures 10a and 10b show that after electrolysis, the dendritic metal nanostructures have completely disappeared from the 90°C and 300°C electrodes and have been replaced by a cracked-mud morphology. EDS mapping (not shown) shows that the cracked-mud consists primarily of Sn oxide, and that the cracks revel the underlying Ti substrate. This morphology is consistent with previous sol-gel reports of NATO.[10] In contrast, the 450°C and 600°C electrodes have generally retained the dendritic morphology.

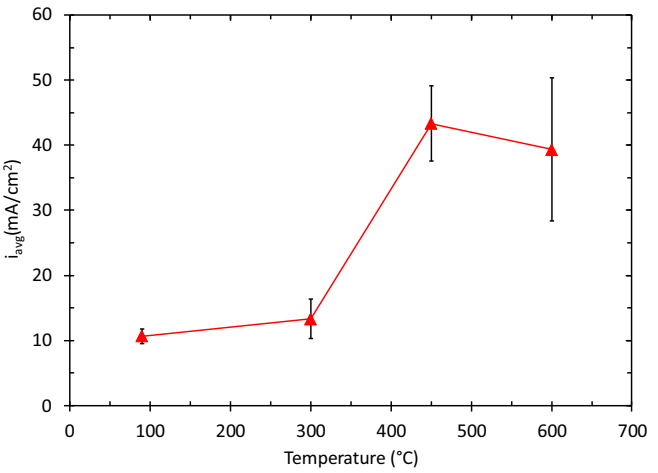

Figure 9. Average current density vs. thermal oxidation temperature with 60 electrodeposition cycles. Measurements reflect the average of three independently synthesized samples. Sol-gel controls at 500°C had an average current density of 60 mA/cm^2.

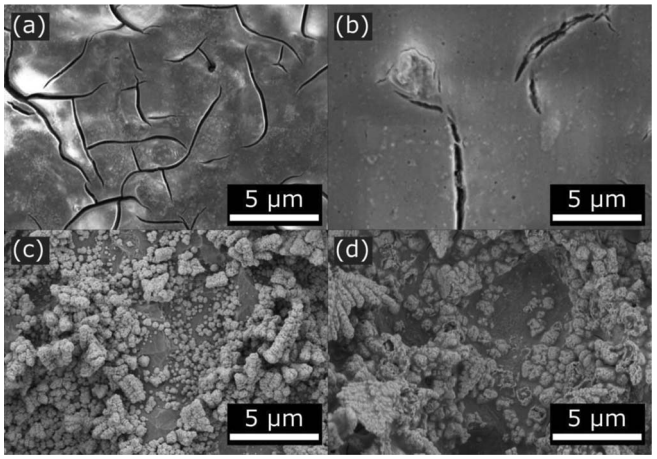

Figure 10. SEM images after ozone production testing for samples in Figure 2 with (a) no thermal oxidation, (b) 300°C, (c) 450°C, and (d) 600°C oxidation. The cracked-mud structure in (a) and (b) show that the dendrites in Figures 2a, 2b had little stability. (d) has less defined moss, and (c) maintains the same morphology as Figure 2c, implying that the 450°C sample was the most stable during polarization.

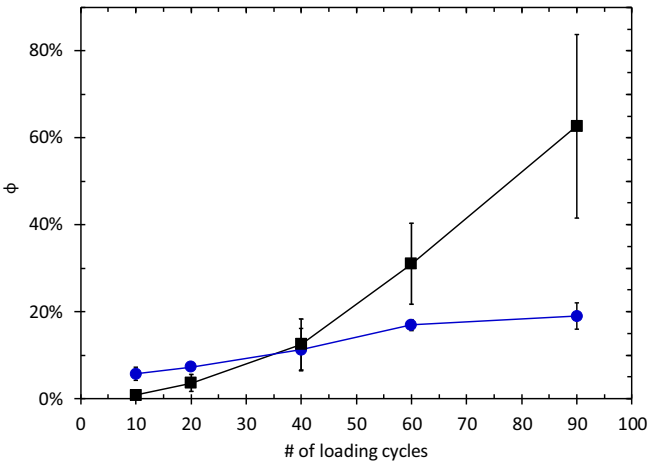

Figure 12. Ozone current efficiency with different amounts of catalyst loading calculated using the in-situ method (black squares) and the indigo method (blue circles). Each sample was thermally oxidized in air at 450°C for two hours.

EDS was used to estimate qualitative bulk compositions before and after testing. Because the peaks for Sb and Sn overlap, only the relative atomic ratio of (Sn+Sb): Ni, is shown. Although Figure 10 shows differences in morphology after testing, EDS in Figure 11 shows qualitatively that all the electrodes lose Ni after polarization at high potential. The instability of Ni in strong acids remains a major challenge in understanding the mechanism of EOP. Despite its well-accepted instability, sub-surface Ni continues to contribute unique catalytic properties to EOP electrodes. Christensen attempted to reconcile these observations by proposing that sub-surface Ni increases the mobility of lattice O in the SnO_2 structure, but such a mechanism does not explain why other metals of similar size and charge do not have the same effect.[31] Sub-surface Ni may also function as a dopant in the SnO_2 structure to modify electronic properties to favor catalytic activity or stability. The catalytic effects of doping on electrochemical activity and selectivity have been observed for many oxide systems.[32,33]

From Figure 10d, the 600°C electrode appears to be less robust than the 450°C (Figure 10c). Cross et al.'s study of Sb-SnO_2 showed that calcination above 400°C resulted in increased Sb surface segregation.[34] Fabbri et al. later investigated duration of Sb- SnO_2 calcination at a fixed temperature and observed a similar effect on stability. Oxides calcined for a longer time had a similar bulk composition but a much higher Sb surface concentration than those calcined for shorter times. After a 1000-cycle CV stability test, the short calcination-time oxides retained their surface and bulk composition while the long calcination-time oxides had a drastic decrease in Sb concentration in both the surface and bulk.[30]

One of the greatest advantages to electrodeposition as a synthetic method for catalysts is the ability to access nanostructures of very high surface area. To vary the surface area, anodes were fabricated with electrodeposition cycles varying from 90, 60, 40, 20, and 10 cycles and oxidized at 450°C. Figures 12 and 13 show that both current density and current efficiency increase with higher loading. The trend of current density is expected, as thicker catalyst layers with higher surface area and thus more sites are expected to have higher activity. However, the trend of current efficiency with catalyst loading has important implications for the EOP mechanism, which is currently not understood.

For surface area to affect selectivity, as well as activity, the reaction must follow a mechanism in which solution-phase intermediates are trapped in catalyst pores, such that they can be further oxidized to the

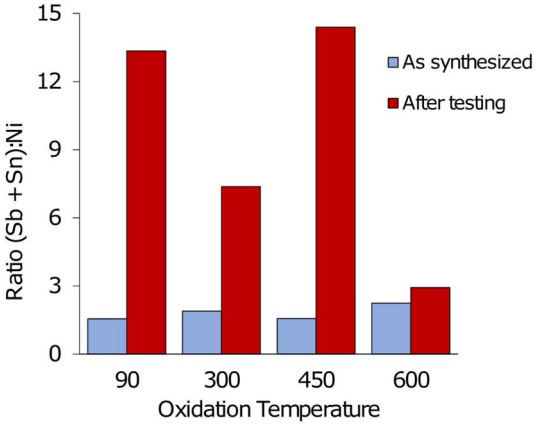

Figure 11. Atomic ratio of (Sn+Sb): Ni, as estimated by EDS, before and after electrochemical testing. There is significant decrease in Ni content at all oxidation temperatures.

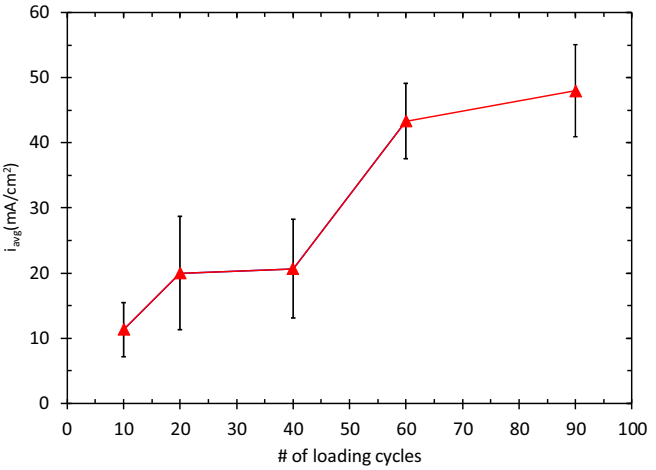

Figure 13. Ozone current density with different numbers of catalyst loading cycles. Each sample was thermally oxidized in air at 450°C for two hours.

final product. This pathway differs from many proposed mechanisms, including recent studies, in which all intermediates are adsorbed on the SnO_2 surface.[12,35,36] However, our findings are consistent with earlier studies on PbO_2 anodes, which have shown that soluble $\cdot OH$ radicals and singlet oxygen are formed when ozone is produced.[35,37] In other applications, thickness-dependent reaction selectivity has been observed for competition between two e^- and four e^- reduction of oxygen to water and peroxide. Bonakdarpour et al.'s study of non-noble oxygen reduction reaction catalysts observed that a catalyst thickness of 20 μg yielded 95% H_2O_2 after oxygen reduction while a thickness of 800 μg yielded only 5%.[39] They concluded that four e^- reduction to H_2O occurs via H_2O_2 and if the catalyst is sparsely loaded, the produced H_2O_2 does not have enough time to be further reduced before it escapes. By the same logic, the electrodeposited NATO thickness dependence observed in Figure 12 supports a solution-mediated O_3 production mechanism via O_2, $\cdot O_2^-$, $\cdot OH$, or some other soluble species.

Conclusions

Thin films of Ni- and Sb- doped SnO_2 (NATO) were synthesized via electrodeposition and thermal oxidation to investigate the utility of this synthesis method for electrochemical ozone production. Electrodeposition yielded metallic Sn and Ni with dendritic morphology. Thermal oxidation of catalysts formed crystalline SnO_2 as well as several NiSn intermetallics. At fixed loading, the resulting catalysts reached a maximum of 31% current efficiency for EOP, consistent with literature. Comparison of the in-situ and indigo methods for ozone quantification suggest that commonly used in-situ methods may be sensitive to inhomogeneities from electrolyte mixing. Low current efficiency at lower oxidation temperatures was attributed to catalyst dissolution and high oxygen activity, while high current efficiency was attributed to the dendritic nanostructure of the catalysts.

Increasing the thickness and loading of the electrodeposited catalysts increased the current efficiency to 63%. The effect of catalyst loading on current efficiency, as well as current density, demonstrates the importance of surface area to catalytic selectivity, thus suggesting that EOP occurs through a solution-mediated mechanism. Identifying these soluble intermediates and the material properties that lead to their formation will likely enable future electrocatalysts to achieve higher activity and selectivity for the EOP reaction.

Acknowledgments

This work was partially supported by NSF-1607991. CML acknowledges support from Drexel University's Office of Undergraduate Research. We thank Aaron Fafarman and Steven Wrenn for use of their laboratory UV-VIS.

ORCID

Maureen H. Tang https://orcid.org/0000-0003-0037-4814

References

1. B. T. Stanley, *Water Cond. Purif. Int.*, 2 (2004).
2. S. D. Han, J. D. Kim, K. Singh, and R. S. Chaundhary, *Indian J. Chem.*, **43A**, 1599 (2004).
3. A. Seidel, *Kirk-Othmer Encycl. Chem. Technol.*, 768 (2004).
4. P. A. Christensen, T. Yonar, and K. Zakaria, *Ozone Sci. Eng.*, **35**, 149 (2013).
5. J. D. Seader and C. Tobias, *Ind. Eng. Chem.*, **44**, 2207 (1952).
6. P. Foller and C. Tobias, *J. Electrochem. Soc.*, **129**, 506 (1982).
7. S. Stucki, G. Theis, R. Kotz, H. Devantay, and H. J. Christen, *J. Electrochem. Soc.*, **132**, 367 (1985).
8. Y.-H. Wang, S. Cheng, K.-Y. Chan, and X. Y. Li, *J. Electrochem. Soc.*, **152**, D197 (2005).
9. P. A. Christensen et al., *Ozone Sci. Eng.*, **31**, 287 (2009).
10. G. Li, Y.-H. Wang, and Q.-Y. Chen, *J. Solid State Electrochem.*, **17**, 1303 (2013).
11. J. B. Parsa, M. Abbasi, and A. Cornell, *J. Electrochem. Soc.*, **159**, D265 (2012).
12. P. A. Christensen et al., *J. Phys. Chem.*, **121**, 1188 (2017).
13. J. Hu et al., *J. Electrochem. Soc.*, **162**, 161 (2015).
14. A. Nemes, I. Fabian, and G. Gordon, *Ozone Sci. Eng.*, **22**, 287 (2000).
15. H. Bader and J. Hoigné, *Water Res.*, **15**, 449 (1981).
16. A. Brenner, *Electrodeposition of Alloys: Principles and Practice*, p. 4, Academic Press, Washington, DC, (1963).
17. C. E. Dube et al., *J. Electrochem. Soc.*, **142**, 3357 (1995).
18. A. J. Bard, R. Parsons, and J. Jordan, *Standard Potentials in Aqueous Solution*, M. Dekker, Editor, p. 1, CRC Press, New York, (1985).
19. J. W. Cuthbertson, N. Parkinson, and H. P. Rooksby, *J. Electrochem. Soc.*, **100**, 107 (1953).
20. H. Leidheiser, I. Czao-Nagy, M. L. Varsanvi, and A. Vertes, *J. Electrochem. Soc.*, **126**, 204 (1979).
21. R. L. Rau and J. C. Bailar, *J. Electrochem. Soc.*, **107**, 745 (1960).
22. A. Merkys et al., *J. Appl. Crystallogr.*, **49** (2016).
23. S. Grazulis, A. Merkys, A. Vaitkus, and M. Okulic-Kazarinas, *J. Appl. Crystallogr.*, **48**, 85 (2015).
24. S. Grazulis et al., *Nucleic Acids Res.*, **40**, D420 (2012).
25. S. Grazulis et al., *J. Appl. Crystallogr.*, **42**, 726 (2009).
26. R. T. Downs and M. Hall-Wallace, *Am. Mineral.*, **88**, 247 (2003).
27. P. A. Christensen, K. Zakaria, H. Christensen, and T. Yonar, *J. Electrochem. Soc.*, **8**, H405 (2013).
28. Y.-H. Wang and Q.-Y. Chen, *Int. J. Electrochem.*, **2013**, 1 (2013).
29. N. Danilovic et al., *J. Phys. Chem. Lett.*, **5**, 2474 (2014).
30. E. Fabbri, A. Rabis, R. Kotz, and T. J. Schmidt, *Phys. Chem. Chem. Phys.*, **16**, 13672 (2014).
31. M. C. Groenenboom et al., *J. Phys. Chem. C*, **121**, 16825 (2017).
32. S. Zou et al., *Chem. Mater.*, **27**, 8011 (2015).
33. K. Saravanan, Y. Basdogan, J. Dean, and J. A. Keith, *J. Mater. Chem. A*, **5**, 11756 (2017).
34. Y. M. Cross and D. R. Pyke, *J. Catal.*, **58**, 61 (1979).
35. L. Da Silva, L. A. De Faria, and J. Boodts, *Electrochem. Acta*, **48**, 699 (2003).
36. G. Gibson, Z. Wang, C. Hardacre, and W.-F. Lin, *Phys. Chem. Chem. Phys.*, **19**, 3800 (2017).
37. D. Wabner and C. Grambow, *J. Electroanal. Chem.*, **195**, 95 (1985).
38. C. Chang, Y. Xu, P. Lu, X. Zhang, and J. Shi, *J. Am. Chem. Soc.*, **139**, 16620 (2017).
39. A. Bonakdarpour et al., *J. Electrochem. Soc.*, **11**, B105 (2008).